nature communications

Article

https://doi.org/10.1038/s41467-026-73259-x

Self sustained oscillations of a nonlinear optomechanical system in the low excitation regime

Received: 19 October 2025

Accepted: 7 May 2026

Published online: 21 May 2026

Check for updates

Shivangi Dhiman[1,7], Korbinian Rubenbauer[2,3,7], Thomas Luschmann[2,3,4], Achim Marx[2], A. Metelmann[1,5,6] & Hans Huebl[2,3,4]

Manifesting across all time, mass and length scales, nonlinearities lie at the core of numerous physical phenomena. Next-generation quantum applications, such as quantum sensing, require the combination of nonlinearity with non-classical correlations. This necessitates the search for an experimental platform which enables a nonlinear response at ultra-low excitation levels in a system with practical sensing potential and quantum compatibility. Here, we report the observation and theoretical modeling of nonlinear dynamics in a mechanical system driven at the single-excitation level. We achieve this using a cavity-optomechanical platform with large single-photon coupling rates and a nonlinear microwave resonator. Specifically, the large Kerr nonlinearity of our superconducting microwave circuit reduces the threshold for the observation of nonlinear dynamics by four orders of magnitude, making this regime experimentally accessible at the few-photon level. The parameter-based quantitative predicative power of the theoretical description underlines our deep understanding of the physics involved and that this device concept paves the way for experiments with non-classical microwave drive schemes.

Nonlinear dynamics is fundamental to both classical and quantum systems. It gives rise to an extremely rich class of physics, like bifurcation[1], chaos[2,3], and synchronization[4,5]. Typically, these phenomena are highly sensitive to initial conditions, requiring a thorough study and a deep understanding to make precise predictions and enable effective use of nonlinear dynamics. While nonlinear systems are ubiquitous in nature, their systematic experimental study often relies on classical mechanical systems or electronic circuits[6,7]. Additionally, nonlinearities also play a substantial role in quantum mechanics and are indispensable for quantum state generation[8–12].

Optomechanical systems parametrically couple an electromagnetic resonator with a mechanical mode, enabling extremely sensitive readout schemes for mechanical sensing applications[13–16]. These systems allow for the monitoring of minute forces originating from, e.g., electromagnetic fields, Bose-Einstein condensates, mass, and even gravitational waves[17,18]. Their extreme sensitivity is linked to the ability to prepare the mechanical mode in the quantum mechanical ground state[19–21] or non-classical states like squeezed states[22–26]. In addition, the same devices are also ideally suited for exploring nonlinear physics both in the classical and quantum domain[27–29]. However, due to the weak optomechanical interaction strength, these systems have been mostly limited to the classical regime up to this point. There have been numerous studies on such nonlinear dynamics in the classical domain, specifically self-sustained oscillations, both from a

[1]Institute for Quantum Materials and Technology, Karlsruhe Institute of Technology, Karlsruhe 76131, Germany. [2]Walther-Meißner-Institut, Bayerische Akademie der Wissenschaften, Walther-Meißner-Straße 8, Garching 85748, Germany. [3]Physics Department, TUM School of Natural Sciences, Technical University of Munich, James-Franck-Straße 1, Garching 85748, Germany. [4]Munich Center for Quantum Science and Technology (MCQST), Schellingstr. 4, Munich 80799, Germany. [5]Institute for Theory of Condensed Matter, Karlsruhe Institute of Technology, Karlsruhe 76131, Germany. [6]Institut de Science et d'Ingénierie Supramoléculaires (ISIS, UMR7006), University of Strasbourg and CNRS, Strasbourg 67000, France. [7]These authors contributed equally: Shivangi Dhiman, Korbinian Rubenbauer. e-mail: anja.metelmann@kit.edu; huebl@wmi.badw.de

theoretical and experimental perspective[30–34]. Most of these works rely on driving the system at high input powers to observe such features. In general, a combination of non-classicality and nonlinear response of the mechanical system can be accessed in the single-photon strong-coupling regime, where the optomechanical coupling rate exceeds the photonic and phononic decay rate. In addition to accessing nonlinear quantum dynamics, this regime allows for the generation of arbitrary quantum states[35–43].

Since entering the single-photon strong-coupling regime is experimentally demanding, suitable schemes need to be explored to reduce the demands on the coupling strength. Promising strategies include enhancing the nonlinearity induced by the optomechanical coupling strength, e.g., by implementing nonlinear elements in the electromagnetic circuit. Inductively coupled cavity-optomechanical systems using superconducting microwave (quantum) circuits with embedded mechanical elements, as demonstrated in refs. 44–47, are ideally suited to test this conjecture. These systems combine an intrinsic nonlinear microwave resonator with a mechanical element and the ability to prepare the mechanical modes close to the ground state[46,48–51].

Here, we experimentally explore and quantitatively model an optomechanical system with a strong nonlinearity implemented as a superconducting quantum circuit. We observe self-sustained oscillations[30–33] of the mechanical oscillator by measuring the scattering response of the nonlinear cavity at excitation levels as low as a few photons. Our semi-classical model quantitatively describes the observed nonlinear response using independently determined system parameters. Notably, the excitation level of the microwave resonator required to trigger self-sustained mechanical oscillations is by several orders of magnitude lower than in conventional optomechanical systems based on linear cavities. The observation of nonlinear features at occupations as low as a few photons makes the setup compatible with future studies in the quantum domain. Specifically, this provides a pathway to investigate nonlinear dynamics driven by non-classical excitation schemes.

Results

Device concept

We use the inductively coupled nano-electromechanical device, which has been described in refs. 44,52. The microwave cavity is frequency tunable between 6.6 and 7.35 GHz by an external magnetic field. It is realized as a superconducting $\lambda/4$ coplanar waveguide (CPW) resonator made from an aluminum thin film (Fig. 1), which is shunted to ground via a dc superconducting quantum interference device (dc-SQUID). The dc-SQUID is partially suspended and hosts two nanomechanical string resonators with a length of 30 µm and resonance frequencies of $\Omega_m/(2\pi) \approx 5.6$ MHz, sharing loss rates of approximately $\Gamma_m/(2\pi) \approx 10$ Hz. It adds a magnetic flux-dependent inductance to the circuit, which allows for tuning of the microwave resonance frequency ω_c, controls the optomechanical single-photon coupling rate g_0, and adds a Kerr nonlinearity $\mathcal{K}$ to the microwave harmonic oscillator. We adjust the applied flux Φ and the total magnetic field B_{ext} using an in-plane and an out-of-plane magnetic field B_{ip} and B_{oop}, respectively. In this paper, we focus on the mechanical mode at $\Omega_m/(2\pi) = 5.607716$ MHz, with large single-photon optomechanical coupling rates g_0 ranging from a few to tens of kilohertz.

This electromechanical device can be accurately modeled using the Hamiltonian for a driven optomechanical system with the addition of a Kerr nonlinearity to the cavity mode[46,48,53],

$$\hat{H}/\hbar = -\Delta\hat{a}^\dagger\hat{a} + \Omega_m\hat{b}^\dagger\hat{b} - \frac{\mathcal{K}}{2}\hat{a}^\dagger\hat{a}^\dagger\hat{a}\hat{a} + g_0\hat{a}^\dagger\hat{a}(\hat{b}+\hat{b}^\dagger). \quad (1)$$

Here, $\hat{a}(\hat{b})$, $\hat{a}^\dagger(\hat{b}^\dagger)$ are the annihilation and creation operators for the cavity (mechanical) mode, and $\Delta = \omega_p - \omega_c$ is the detuning in the frame rotating with respect to the external microwave probe frequency ω_p. Note that ω_c is the resonance frequency of the nonlinear cavity at very small driving strength, i.e., in its linear regime.

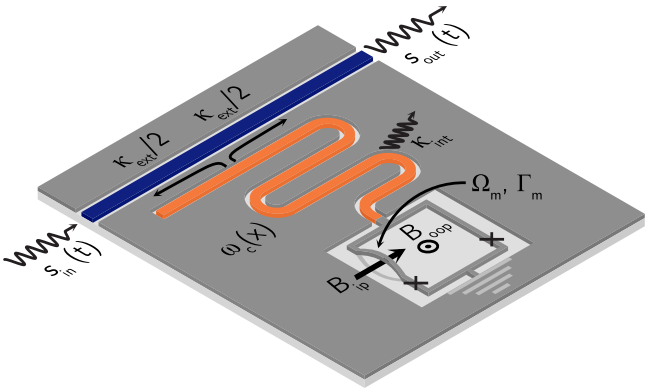

Fig. 1 | Schematic representation of the examined device. The device features a superconducting flux-tunable $\lambda/4$ coplanar waveguide (CPW) resonator (orange), which is shunted to ground via a dc-SQUID. Signal input $s_{in}(t)$ and output $s_{out}(t)$ are achieved through a transmission line (blue). The dc-SQUID is partially suspended, forming two nanomechanical string resonators (only one of which is depicted here). The frequency of the microwave resonator is tunable via an out-of-plane magnetic field B_{oop}. The application of an in-plane magnetic field B_{ip} induces an optomechanical coupling between the out-of-plane displacement of the nanostring and the CPW resonator. The sample is probed at a temperature of 70 mK in a commercial dilution refrigerator. Details on the device fabrication and cryogenic wiring can be found in the "Methods" section.

Stability analysis

Since self-sustained oscillations are a signature of instability in the mechanical mode, we first discuss the stability of our system as a function of the detuning Δ and the input photon flux n_{in}. For this analysis, we solve for the fixed points of the system and perform a linear stability test in their proximity[7] (Supplementary Note 7). Generally, such an optomechanical system has one or three real solutions for fixed points[34] depending on n_{in} and Δ. This is because the number of physical (real) solutions to the fixed-point equation is governed by a cubic equation, which can have either 1 or 3 real solutions depending on the parameters. If the real part of all the eigenvalues of the stability (drift) matrix is negative, then the corresponding fixed point is stable.

Figure 2 compares the resulting stability diagram of our electromechanical system with and without a non-zero Kerr and optomechanical interaction, where we normalized the input photon flux in all cases to the same critical photon flux $n_{in,crit} = 2\kappa^3/(3\sqrt{3}\kappa_{ext}\mathcal{K}_{eff})$ calculated for $\mathcal{K}, g_0 \neq 0$. Here, the effective Kerr constant $\mathcal{K}_{eff} = \mathcal{K} + \mathcal{K}_m$ is composed of the intrinsic nonlinearity of the superconducting circuit $\mathcal{K}$ and the nonlinearity originating from the radiation pressure of the mechanical mode $\mathcal{K}_m$[48,54]. While the case of a linear cavity, $\mathcal{K} = 0$ in Fig. 2a, c, shares features like multi-stability with that of a nonlinear cavity, $\mathcal{K} \neq 0$ in Fig. 2b, d, e, a non-zero $\mathcal{K}$ value dramatically reduces the excitation powers required to enter this regime. In particular, the non-zero Kerr nonlinearity shifts the transition from at least one stable (regions ii-iv) to one unstable (region i) fixed point towards negative detunings (i.e., the red sideband) for very low intra-cavity photon occupations. Because the cavity resonance shifts towards negative detunings due to the strong Kerr nonlinearity, the effective sidebands also shift with power, enabling an effective heating of the mechanical mode at negative detunings. Moreover, the multi-stable area (regions iii, iv), with three fixed points, is accessible at several orders of magnitude lower input powers than in a linear optomechanical system. We can understand this by the critical photon flux that quantifies the boundary where our system becomes

https://doi.org/10.1038/s41467-026-73259-x

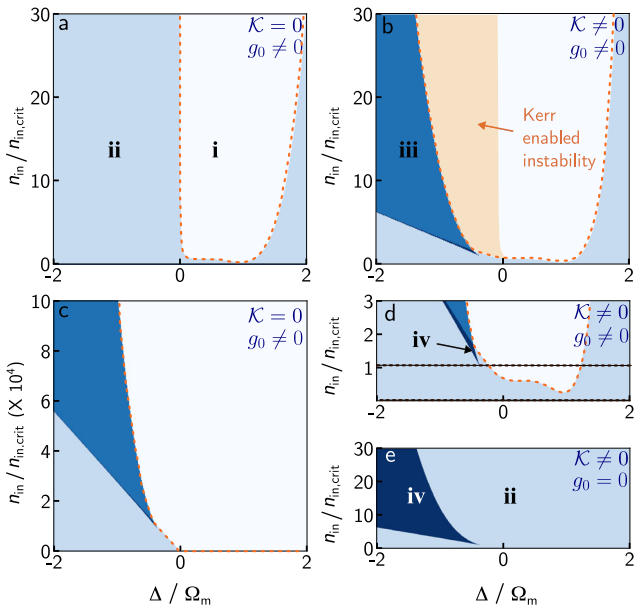

Fig. 2 | Stability diagram of a (non)linear optomechanical system. The system is described by Eq. (1) as a function of the normalized detuning of the probe frequency from the cavity resonance, Δ/Ω_m, and the input photon flux n_{in} normalized with respect to the critical photon flux $n_{in,\,crit}$ at which the optomechanical system becomes bistable. On the left, panels **a** and **c** show a linear system with $\mathcal{K} = 0$, whereas in panels **b**, **d**, and **e** on the right, a Kerr nonlinearity of $\mathcal{K}/2\pi = 70$ kHz is assumed. For all panels with non-zero coupling, $g_0/2\pi = 4.69$ kHz. $n_{in,crit}$ is the same in all panels and calculated for the case of $\mathcal{K}/2\pi = 70$ kHz. It corresponds to an input power of −120 dBm, where the cavity starts to bifurcate at an occupation of $\bar{n}_{c,\,crit} = 19$. These parameter values correspond to parameter set III in the experiment (Table 1). The colors depict stability regions with different amounts of (un) stable solutions. In region i, we find one unstable, in ii one stable, in iii one stable and two unstable, and in iv two stable and one unstable fixed point. Unstable regions are encircled by a dashed orange line. In **b**, the cavity nonlinearity induces a Kerr-enhanced instability, extending the unstable region compared to a linear system (orange shaded area). Note that panel **c** extends **a** to vastly larger input powers. Only then one can observe multi-stability in a linear system, whereas the Kerr nonlinearity reduces the input power required to reach this regime by four orders of magnitude. Panel **d** is a zoom into the low power region of **b**, where the dashed horizontal lines represent the input powers displayed in Fig. 3c,d. Panel **e** shows the phase diagram for a classical nonlinear duffing resonator with zero optomechanical interaction $g_0 = 0$.

multistable, which is a nonlinear phenomenon. The critical photon flux $n_{in,crit}$ is determined by the effective Kerr $\mathcal{K}_{eff}$. For our system parameters in Fig. 2, $\mathcal{K}_m \approx 10^{-4}\mathcal{K}$, which means that the critical input power is roughly four orders of magnitude smaller compared to a linear cavity. Hence, the finite Kerr nonlinearity qualitatively alters the stability diagram as displayed in Fig. 2a, b. For large positive detunings, the system is forced back into stability for $\mathcal{K}\neq 0$ by the Kerr nonlinearity, whereas for $\mathcal{K} = 0$ this boundary is only determined by Δ and g_0. By setting $g_0 = 0$ as in Fig. 2e, we recover the phase diagram of a classical Kerr nonlinear resonator with three fixed points (two stable and one unstable, region iv).

We can intuitively understand the qualitative form of the stability diagram. The region with one unstable fixed point links to the possibility of stimulating self-sustained oscillations of the mechanical system using a blue sideband drive (region i). The multiple fixed points originate from the total Kerr nonlinearity of the system, with contributions from the microwave circuit and the optomechanical interaction[48].

Within the stability diagrams shown in Fig. 2 we can identify the following bifurcations: (i) a Hopf bifurcation at the transition between a stable and an unstable fixed point (boundary between region i and ii) and the same transition when involving a total of three fixed points (transition from region iv to iii); (ii) a (inverse) saddle node bifurcation occurring between areas with three and a single fixed point (transition from ii to iv, and from iii to i). More details can be found in Supplementary Note 7.

Cavity scattering response

To link the stability diagram to the experimental data, we model the scattering response of the microwave resonator $S_{21} = s_{out}/s_{in}$ in different stability regimes using two approaches: an approximative analytical model and the full numerical solution of the equations of motion of the system, both of which are discussed in Supplementary Note 6. Both approaches employ standard input-output theory[55] to obtain the cavity response. For the analytical description, we distinguish between the responses obtained in the stable and unstable regions. When the system is stable, the scattering response S_{21} is given by

$$S_{21} = 1 - \frac{\kappa_{ext}}{2}\frac{1}{-i(\Delta + \mathcal{K}_{eff}\bar{n}_c) + \kappa/2}. \tag{2}$$

Here, $\kappa = \kappa_{ext} + \kappa_{int}$ is the total loss rate of the microwave resonator with the coupling rate κ_{ext} and the internal loss rate κ_{int}, and $\bar{n}_c$ is the steady state photon occupation of the microwave cavity.

In the regime of instability, we solve the classical equations of motion assuming a coherent oscillation of the mechanical mode with $\beta = \bar{\beta} + B'e^{-i\phi}e^{-i\Omega_m t}$, where $\bar{\beta}$ represents the static displacement of the mechanical resonator and B' (ϕ) are the amplitude (phase) associated with the oscillations of the mechanical displacement[31,32]. B' is determined via the power balance condition $\Gamma_m + \Gamma_{opt} = 0$ with the optomechanical damping rate Γ_{opt}[56]. The scattering response in this regime is

$$S_{21} = 1 - \frac{\kappa_{ext}}{2}\sum_n \frac{J_n(z_1)J_n(z_1)}{-i(\Delta + \mathcal{K}_{eff}\bar{n}_c + n\Omega_m) + \kappa/2}, \tag{3}$$

with J_n the Bessel function of the first kind and $z_1 = 2B'g_0/\Omega_m$.

In addition, we simulate the system's response by numerically solving the equations of motion for our Hamiltonian and using the input-output relation to obtain the scattering response. The simulation fully captures the dynamic evolution of the correct photon number without assuming a steady state, as done in the analytical model. This allows the correct incorporation of the Kerr nonlinearity's effect, especially at the transition boundary between stable and unstable dynamics. Furthermore, we can precisely predict the time required for the system to reach its steady state (see Supplementary Note 6.2 for more details). Note that we have restricted the discussion to classical dynamics and thus have not investigated quantum fluctuations since our single-tone measurement only gives access to the mean-field scattering response of the system.

Pulsed measurement technique to avoid transient dynamics

For the experiment, we apply a combination of in-plane and out-of-plane magnetic fields. This sets the single-photon coupling rate $g_0 = (\partial_\Phi\omega_c)\gamma B_{ext}x_{zpf}l$[44,45] and the intrinsic Kerr nonlinearity $\mathcal{K}$ of the cavity (Table 1, and SI). Here, $\partial_\Phi\omega_c = \partial\omega_c/\partial\Phi$ is the flux responsivity, i.e., the derivative of the cavity resonance frequency with respect to the applied flux Φ, γ is the mode shape factor, and l is the length of the nanostring.

Specifically, we set $B_{ip} = 30$ mT for all experiments presented and control g_0 between zero and several tens of kilohertz using Φ_{oop} via $\partial_\Phi\omega_c \approx \partial_{\Phi_{oop}}\omega_c$. Notably, Φ_{oop} also affects the Kerr nonlinearity $\mathcal{K}$ of the cavity. Thus, by adjusting the out-of-plane magnetic field B_{oop} or Φ_{oop}, we are able to explore a wide range of system parameters

https://doi.org/10.1038/s41467-026-73259-x

Table 1 | Experimental system parameters

	Set II	Set III	Set IV
$\omega_c/2\pi$ (GHz)	7.310	7.241	7.006
$\kappa_{int}/2\pi$ (MHz)	0.60	0.68	2.33
$\kappa_{ext}/2\pi$ (MHz)	1.72	1.64	1.55
$\mathcal{K}/2\pi$ (kHz)	20	70	1.4×10^3
$\bar{n}_{c,crit}$	67	19	1.6
$\Omega_m/2\pi$ (MHz)	5.607653	5.607483	5.607110
$\Gamma_m/2\pi$ (Hz)	14	12	6
$g_0/2\pi$ (kHz)	1.95	4.69	18.4
$g_0/\mathcal{K}$	0.10	0.07	0.01

The sets of system parameters are determined independently at the working points and used as input to the analytical model and the numerical simulation of the scattering response. Additional parameter sets are discussed in Supplementary Note 4. Since the actual occupation of the nonlinear microwave cavity depends on the detuning Δ, we give the cavity occupation at bifurcation and at the critical detuning as $\bar{n}_{c,crit} = \kappa/\sqrt{3}\mathcal{K}_{eff}$ as a reference. Note that due to the tunability of our microwave cavity, we are able to cover substantially different values of g_0, $\mathcal{K}$, and thus also the ratio $g_0/\mathcal{K}$.

(Table 1). To demonstrate our quantitative understanding of the response, we determine the system parameters for four distinct working points using independent techniques as discussed in Supplementary Note 1. Those then serve as input parameters for our theoretical model, which we compare with the experimental data.

To explore the stability diagram and the dynamic response of the system experimentally, we apply a single fixed frequency microwave tone at ω_p to the system ($s_{in}(t)$) and record the response in the time domain ($s_{out}(t)$) (Figs. 3a, b and 1) in the form of a time-dependent complex transmission parameter $S_{21}(t)$. The tone is applied, and $S_{21}(t)$ is recorded for 1.4 s to experimentally measure the ring-up of the mechanics and verify that the steady state is reached. To display the transmission parameter only in the steady state, $S_{21}(t)$ is averaged over the last 2 ms of the pulse. This ensures that it is not altered by transient or ring-up effects, which occur initially after the probe pulse is applied. Between subsequent interrogations, we allow the system to equilibrate with its thermal environment for 0.8 s, so that any mechanical excitation fully depletes before the next pulse is applied. We repeat this procedure as a function of the frequency of the microwave tone ω_p. A full $S_{21}(\omega, t)$ spectrum can be found in Supplementary Note 3. Figure 3c, d shows the resulting steady state transmission as a function of frequency for two different excitation powers P_d at the cavity. This measurement protocol is essential to compare the experimental data with theory. Since our system is weakly dissipative ($\kappa < \Omega_m$) along with $g_0 < \Omega_m$, it can require up to 1 s to reach the steady state after the probe tone is applied, which we observe both in the simulation and the experiment. Hence, conventional frequency swept experiments can result in a transient behavior, which is beyond the scope of our theoretical treatment (for more details, see Supplementary Note 3). We chose this measurement protocol since it is a conceptually simple and fast measurement with good signal-to-noise at the given bandwidths and powers. Moreover, it allows for a direct comparison with our theoretical framework. A measurement of the self-sustained oscillations by the temporal behavior of the microwave output power, as done in, e.g., ref. 30, is impractical due to the low power levels in our study.

Connecting experiment, model and stability analysis

Figure 3c, d show the steady state transmission data for $P_d = -139.6$ and -118.6 dBm, which correspond to $n_{in}/n_{in,crit} = 0.008$ and 1.10, respectively. The power at the sample is calibrated as detailed in Supplementary Note 2. The data recorded with the low excitation power shows the expected linear response of the microwave resonator. Surprisingly, even a moderate excitation level of only

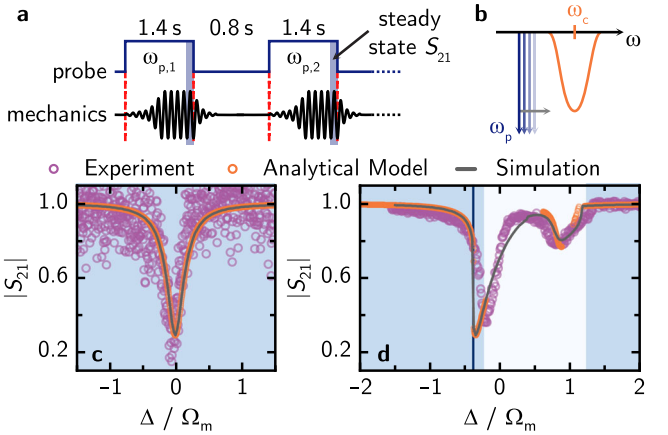

Fig. 3 | Measurement protocol and results. a Measurement protocol in the time domain: A probe signal at a given frequency $\omega_{p,1}$ is applied sufficiently long for the mechanical oscillator to ring up and reach its steady state. A waiting period follows, which allows the excitation to ring down completely. We repeat this for different frequencies $\omega_{p,2}$, $\omega_{p,3}$, ... of the probe signal. The detuning Δ is calculated for each probe frequency with respect to the resonance frequency ω_c of the cavity in the linear regime, i.e. $\Delta = \omega_{p,i} - \omega_c$ for $i = 1, 2, 3, \ldots$. **b** Measurement protocol in the frequency domain: A single microwave probe/pump tone with frequency ω_p is swept around the cavity resonance ω_c. We measure its complex scattering parameter $S_{21} \propto s_{out}/s_{in}$. **c**, **d** Scattering response $|S_{21}|$ observed in the experiment (purple dots), calculated with our analytical model (orange dots), and obtained from numerical simulation (gray lines) for parameter set III and an input power of $n_{in}/n_{in,crit} = 0.008$ and 1.10 corresponding to $P_d = -139.6$ dBm and -118.6 dBm, respectively. The different stability regions are highlighted in the background by the color code introduced in Fig. 2. We see that both the analytical model and the simulation capture the nonlinear features, including the self-sustained oscillations observed as an additional absorption dip around $\Delta/\Omega_m = 1$ in **d**.

$P_d = -118.6$ dBm qualitatively alters the transmission signature in two ways by (i) deforming the main resonance and shifting it to negative detunings and (ii) the appearance of an additional absorption signature of the microwave cavity at frequencies corresponding to the blue sideband around $\Delta/\Omega_m = 1$.

We quantitatively understand both excitation scenarios analytically using Eqs. (2) and (3) to compute the scattering response. In the first case shown in Fig. 3c, the input is much below the critical input power $n_{in,crit}$, such that the system is completely stable and can be correctly described using Eq. (2). This allows us to assert that we only have a single stable fixed point and thus only one photon branch exists for all detunings (corresponding to region ii).

For higher powers as in Fig. 3d, the analytically modeled response is piecewise combined using the stability diagram shown in Fig. 2d. The scattering response in regions ii-iv with at least one stable fixed point is computed using Eq. (2), which already includes the shift of the transmission minimum due to the finite Kerr nonlinearity. Transitioning into region i, the system undergoes a Hopf bifurcation, which characterizes the onset of self-sustained oscillations of the mechanical mode[7], hence, we model the scattering response in this region with Eq. (3). In this range, we find further absorption signatures at multiples of the mechanical resonance frequency and frequencies higher than the response of the microwave cavity.

Notably, this spectral signature shows a Duffing-like shape similar to the main resonance, as it is slightly skewed and shifted from the first mechanical sideband to lower frequencies. This is again due to the Kerr nonlinearity and is correctly reflected in our model. In addition, we operate in Fig. 3d above bifurcation, causing the photon branches to split into three. This corresponds to three fixed points, as in regions iii, iv, similar to the three photon branches of a Duffing oscillator. For smaller values of g_0, there are two stable (upper/lower) and one

https://doi.org/10.1038/s41467-026-73259-x

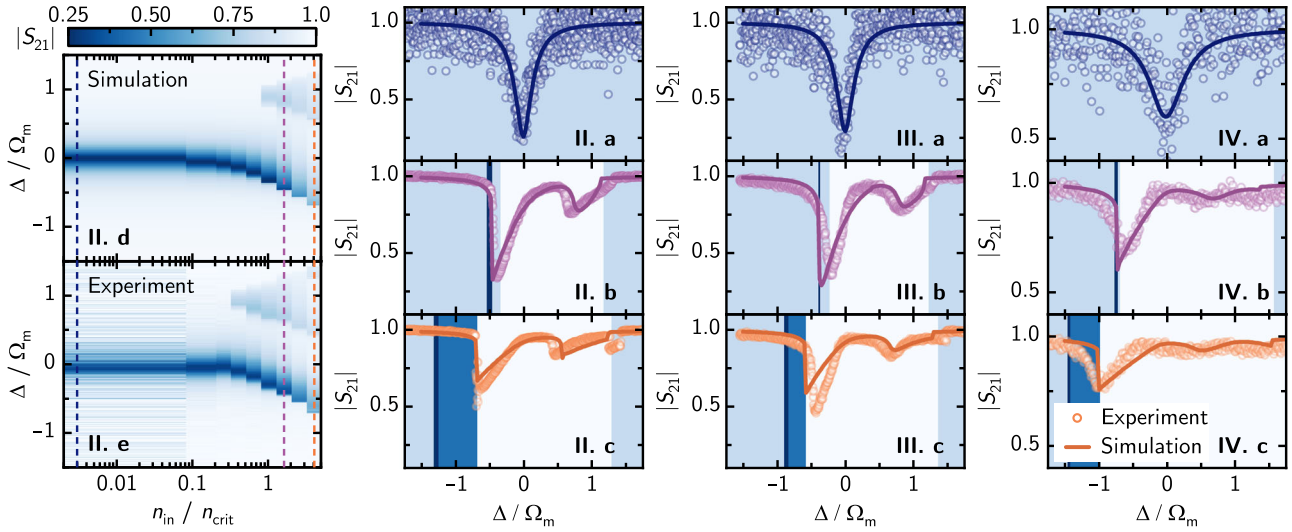

Fig. 4 | Power and parameter dependence of the cavity scattering response. The panels are labeled with capital Roman numbers according to the parameter sets, so that, e.g. the leftmost two columns **II.a**–**e** refer to parameter set II in Table 1. The two color plots **II.d**, **e** compare simulation and experiment for a wide set of input powers. The linecuts in **II.a**–**c** show the experimental data (points) and numerical simulation (lines) for a single input power increasing from top to bottom. The powers are indicated by the dashed vertical lines in **II.d**, **e** and correspond to $n_{in}/n_{in,crit}$ = 0.003, 1.63, and 4.09, translating to P_d = − 139.6 dBm, − 111.6 dBm, and − 107.6 dBm. For **III a**–**c**, where both g_0 and $\mathcal{K}$ are increased, we show $n_{in}/n_{in,crit}$ = 0.008, 1.10, and 2.77 (P_d = − 139.6 dBm, − 118.6 dBm, and − 114.6 dBm). Since **IV a**–**c** On the right, it has the largest single-photon coupling g_0 and Kerr nonlinearity $\mathcal{K}$, the lowest absolute input powers are required for the additional absorption dips to appear on the blue sideband. Input powers of $n_{in}/n_{in,crit}$ = 0.04, 1.45, and 2.88 are depicted, which correspond to P_d = − 139.6 dBm, − 123.6 dBm, and − 120.6 dBm. For all linecuts, the background is shaded according to the color code introduced with the stability diagram in Fig. 2.

unstable (middle) photon branch as indicated by region iv. However, our system settles for nearly all detunings into the lower photon branch since the instability of the mechanical subsystem makes the upper branch inaccessible, corresponding to region iii with only one stable and two unstable fixed points. For more details, we refer to Supplementary Note 7.

While our analytical model provides a good quantitative understanding of the system, it inherently includes approximations, such as the assumption of a stationary cavity state, and neglects excitation of the mechanical mode by higher-order sidebands. In addition, these constrain the model to finite frequency sections. Therefore, we also numerically solve the equations of motion to obtain the scattering response displayed in Fig. 3c, d, and find excellent quantitative agreement between experiment, analytical model, and simulation.

Extending to various powers and system parameters

Figure 4 compares the input power-dependent spectral data with the numerical model for the parameter sets given in Table 1, demonstrating our exquisite quantitative understanding. For these datasets, we repeat our transmission measurement for different input powers and detunings and display the steady state results as $|S_{21}|$. As predicted by the stability diagram and Eqs. (2) and (3), we observe a shift of the microwave resonator frequency to lower frequencies combined with a distorted Duffing-like lineshape for all three sets of parameters. In addition, we find a second absorption dip in the blue detuned regime, which shows a threshold behavior with the input power. As before, we attribute this feature to self-sustained oscillations of the mechanical mode observed through the cavity response and created by the effective blue-sideband drive of the applied tone. Thus, they reflect the system's instability at these driving powers. This unique feature of our optomechanical system is linked to the comparably large g_0 and $\mathcal{K}$ values. All spectral features and their power dependence are in excellent agreement with the parameter-based, fit-free simulation. Line cuts at different input powers (Fig. 4a–c for set II, III, and IV) underline this aspect. Only at very high input powers do we notice a slight deviation in absorption strength. This deviation might arise due to various reasons. First, the microwave drive induces a thermal occupation of the system that our model does not account for. Second, the systems parameters might change at high input powers. In particular, a reduction of the loss rate κ of the cavity due to the saturation of two-level systems can quickly influence the dip shape. Third, uncertainties in the power calibration might have a larger influence at larger drive powers. Lastly, higher-order nonlinearities, which are not included in our theoretical model, could also come into play at these powers.

Furthermore, the fixed point analysis quantitatively maps out the areas with different types and amounts of fixed points. The corresponding boundaries between stable and unstable regions are reflected experimentally, for example, as the sudden jump observed at the high-frequency end of the sidedip around $\Delta/\Omega_m \approx 1.4$ in Fig. 4II.c and III.c. Hence, for larger positive detunings, we do not observe or expect additional absorption features as our system remains stable.

Discussion

Additional datasets presented in Supplementary Note 4 underline the quantitative agreement between experiment and model. Between these, the changing single-photon optomechanical coupling g_0 shifts the instability barrier. For higher g_0, the sidebands appear already at lower input powers. This shows that, even though both the optomechanical coupling g_0 and the Kerr nonlinearity $\mathcal{K}$ strongly influence the stability regions and steady state times, we can model the nonlinear response to great quantitative agreement. Note that due to the large Kerr, the photon number in the cavity, at which we observe these strongly nonlinear physics, is in the range of only a few to tens of photons ($\overline{n}_c \approx 2 - 120$).

In conclusion, we have observed self-sustained oscillations in a nonlinear nano-electromechanical device and demonstrated excellent quantitative understanding between our theory and experiment. While our theoretical analysis is restricted to the classical domain, the presence of such nonlinear features like limit cycles or period doubling[33]

marks the threshold for the parameter space where nonlinear interactions in the system become dominant. There are theoretical proposals predicting non-classical states in such regimes[41], but they require the still experimentally challenging single-photon strong coupling. Notably, the introduction of a nonlinear microwave resonator into our nano-electromechanical system drastically reduces the threshold for nonlinear dynamics to the few-photon level and hereby enables a potential pathway for the generation of non-classical states and the study of their dynamics in the nonlinear regime (Supplementary Note 5). Both require the mechanical mode to be close to or in its ground state, which can be achieved by red sideband cooling. Additionally, the Kerr nonlinearity can be engineered as desired to explore potential pathways for state generation. Beyond the fundamental aspects, potential novel applications in quantum sensing envisage the nonlinear dynamics of non-classical states as a resource[57], which come in reach given our findings combined with the versatile toolbox of superconducting quantum circuits.

Methods

Device fabrication

The device is structured on a high-resistivity silicon wafer ($R > 10\,\mathrm{k\Omega}$ cm), from which a 6 x 10 mm chip is diced. The entire layout is defined in a single step using electron beam lithography. Subsequently, a 40 nm thick aluminum film is evaporated in a shadow-angle configuration, followed by oxidation, and then a deposition of a secondary 70 nm thick aluminum film. The structure is then transferred onto the substrate through a lift-off process. To obtain tensile stressed aluminum, the entire chip is annealed for 30 min at 350 °C under atmospheric pressure. Following this, selective removal of the silicon beneath the aluminum is performed using reactive-ion etching (RIE), leaving two suspended and mechanically compliant nanostrings within the dc-SQUID. For further details on the fabrication process and detailed scanning electron microscopy (SEM) images, we refer to ref. 44.

Cryogenic Wiring

Since all experiments presented here are conducted at millikelvin temperatures in a commercial dilution refrigerator, cryogenic microwave wiring is required to access the sample. The input microwave line is equipped with a total of 50 dB of attenuation before reaching the device under test (DUT) to suppress thermal noise and unwanted reflections. The output signal is amplified by a high-electron-mobility transistor (HEMT), which is mounted at the 4 K stage. To prevent back reflections from the amplifier, three microwave circulators are placed between the DUT and the HEMT. In addition to the microwave wiring, a DC current line allows to control the current through a superconducting coil mounted outside of the DUT package. This allows for the adjustment of the applied out-of-plane magnetic field B_{oop}, which tunes the resonance frequency of the microwave cavity by modifying the effective Josephson inductance of the dc-SQUID. The large in-plane magnetic field B_{ip} is generated by a commercial 3D vector magnet, in the center of which the DUT with the small coil is placed.

Data availability

The raw data that supports the findings of this study is available from the corresponding author upon reasonable request. Processed data representing all the data in the published figures, both from the main text and the Supplementary Information, are openly available in the zenodo repository[58] under the following https://doi.org/10.5281/zenodo.18954807.

Code availability

The code used for numerical simulation is openly available in the Zenodo repository[59]. The code is also made available on GitHub under the following url: https://github.com/dhiman-shivangi/self-oscillations-optomechanics-codes.

References

1. Howard, L.N., Kopell, N. A translation of Hopf's original paper. In: Marsden, J.E., McCracken, M. (eds.) The Hopf Bifurcation and Its Applications vol. 19, pp. 163–193. Springer, New York, NY. Chap. 5 (1976).
2. Bakemeier, L., Alvermann, A. & Fehske, H. Route to chaos in optomechanics. *Phys. Rev. Lett.* **114**, 013601 (2015).
3. Lü, X.-Y., Jing, H., Ma, J.-Y. & Wu, Y. $\mathcal{PT}$-Symmetry-Breaking Chaos in Optomechanics. *Phys. Rev. Lett.* **114**, 253601 (2015).
4. Jensen, R. V. Synchronization of randomly driven nonlinear oscillators. *Phys. Rev. E* **58**, 6907–6910 (1998).
5. Amitai, E., Lörch, N., Nunnenkamp, A., Walter, S. & Bruder, C. Synchronization of an optomechanical system to an external drive. *Phys. Rev. A* **95**, 053858 (2017).
6. Dykman, M. (ed.): Fluctuating Nonlinear Oscillators: From Nanomechanics to Quantum Superconducting Circuits. Oxford University Press, Oxford, United Kingdom (2012).
7. Strogatz, S. Nonlinear Dynamics and Chaos: With Applications to Physics, Biology, Chemistry, and Engineering, Third edition edn. CRC Press, Boca Raton, London, New York (2019).
8. Yurke, B. & Stoler, D. Generating quantum mechanical superpositions of macroscopically distinguishable states via amplitude dispersion. *Phys. Rev. Lett.* **57**, 13–16 (1986).
9. Hofheinz, M. et al. Synthesizing arbitrary quantum states in a superconducting resonator. *Nature* **459**, 546–549 (2009).
10. Vlastakis, B. et al. Deterministically encoding quantum information using 100-photon schrödinger cat states. *Science* **342**, 607–610 (2013).
11. Puri, S., Boutin, S. & Blais, A. Engineering the quantum states of light in a Kerr-nonlinear resonator by two-photon driving. *npj Quantum Inf* **3**, 1–7 (2017).
12. He, X. L. et al. Fast generation of Schrödinger cat states using a Kerr-tunable superconducting resonator. *Nat Commun* **14**, 6358 (2023).
13. Aspelmeyer, M., Kippenberg, T. J. & Marquardt, F. Cavity optomechanics. *Rev. Mod. Phys.* **86**, 1391–1452 (2014).
14. Barzanjeh, S. et al. Optomechanics for quantum technologies. *Nat. Phys.* **18**, 15–24 (2022).
15. Metcalfe, M. Applications of cavity optomechanics. *Applied Physics Reviews* **1**, 031105 (2014).
16. Li, B.-B., Ou, L., Lei, Y. & Liu, Y.-C. Cavity optomechanical sensing. *Nanophotonics* **10**, 2799–2832 (2021).
17. Brennecke, F., Ritter, S., Donner, T. & Esslinger, T. Cavity optomechanics with a Bose-Einstein condensate. *Science* **322**, 235–238 (2008).
18. LIGO Scientific Collaboration and Virgo Collaboration Observation of Gravitational Waves from a Binary Black Hole Merger. *Phys. Rev. Lett.* **116**, 061102 (2016).
19. Chan, J. et al. Laser cooling of a nanomechanical oscillator into its quantum ground state. *Nature* **478**, 89–92 (2011).
20. O'Connell, A. D. et al. Quantum ground state and single-phonon control of a mechanical resonator. *Nature* **464**, 697–703 (2010).
21. Teufel, J. D. et al. Sideband cooling of micromechanical motion to the quantum ground state. *Nature* **475**, 359–363 (2011).
22. Wollman, E. E. et al. Quantum squeezing of motion in a mechanical resonator. *Science* **349**, 952–955 (2015).
23. Pirkkalainen, J.-M., Damskägg, E., Brandt, M., Massel, F. & Sillanpää, M. A. Squeezing of quantum noise of motion in a micromechanical resonator. *Phys. Rev. Lett.* **115**, 243601 (2015).
24. Barzanjeh, S. et al. Stationary entangled radiation from micromechanical motion. *Nature* **570**, 480–483 (2019).

25. Lecocq, F., Clark, J. B., Simmonds, R. W., Aumentado, J. & Teufel, J. D. Quantum nondemolition measurement of a nonclassical state of a massive object. *Phys. Rev. X* **5**, 041037 (2015).
26. Barzanjeh, S. et al. Mechanical on-chip microwave circulator. *Nat Commun.* **8**, 953 (2017).
27. Huber, J. S. et al. Spectral evidence of squeezing of a weakly damped driven nanomechanical mode. *Phys. Rev. X* **10**, 021066 (2020).
28. Ochs, J. S. et al. Frequency comb from a single driven nonlinear nanomechanical mode. *Phys. Rev. X* **12**, 041019 (2022).
29. Kuang, T. et al. Nonlinear multi-frequency phonon lasers with active levitated optomechanics. *Nat. Phys.* **19**, 414–419 (2023).
30. Carmon, T., Rokhsari, H., Yang, L., Kippenberg, T. J. & Vahala, K. J. Temporal behavior of radiation-pressure-induced vibrations of an optical microcavity phonon mode. *Phys. Rev. Lett.* **94**, 223902 (2005).
31. Marquardt, F., Harris, J. G. E. & Girvin, S. M. Dynamical multistability induced by radiation pressure in high-finesse micromechanical optical cavities. *Phys. Rev. Lett.* **96**, 103901 (2006).
32. Krause, A. G. et al. Nonlinear radiation pressure dynamics in an optomechanical crystal. *Phys. Rev. Lett.* **115**, 233601 (2015).
33. Das, S. R. et al. Instabilities near ultrastrong coupling in a microwave optomechanical cavity. *Phys. Rev. Lett.* **131**, 067001 (2023).
34. Roque, T. F., Marquardt, F. & Yevtushenko, O. M. Nonlinear dynamics of weakly dissipative optomechanical systems. *New J. Phys.* **22**, 013049 (2020).
35. Clerk, A. A., Marquardt, F. & Harris, J. G. E. Quantum measurement of phonon shot noise. *Phys. Rev. Lett.* **104**, 213603 (2010).
36. Liu, Y. -x et al. Qubit-induced phonon blockade as a signature of quantum behavior in nanomechanical resonators. *Phys. Rev. A* **82**, 032101 (2010).
37. Nunnenkamp, A., Børkje, K. & Girvin, S. M. Single-photon optomechanics. *Phys. Rev. Lett.* **107**, 063602 (2011).
38. Rabl, P. Photon blockade effect in optomechanical systems. *Phys. Rev. Lett.* **107**, 063601 (2011).
39. Qian, J., Clerk, A. A., Hammerer, K. & Marquardt, F. Quantum signatures of the optomechanical instability. *Phys. Rev. Lett.* **109**, 253601 (2012).
40. Kronwald, A. & Marquardt, F. Optomechanically induced transparency in the nonlinear quantum regime. *Phys. Rev. Lett.* **111**, 133601 (2013).
41. Nation, P. D. Nonclassical mechanical states in an optomechanical micromaser analog. *Phys. Rev. A* **88**, 053828 (2013).
42. Hauer, B. D., Metelmann, A. & Davis, J. P. Phonon quantum nondemolition measurements in nonlinearly coupled optomechanical cavities. *Phys. Rev. A* **98**, 043804 (2018).
43. Hauer, B. D., Combes, J. & Teufel, J. D. Nonlinear sideband cooling to a cat state of motion. *Phys. Rev. Lett.* **130**, 213604 (2023).
44. Schmidt, P. et al. Sideband-resolved resonator electromechanics based on a nonlinear Josephson inductance probed on the single-photon level. *Commun. Phys.* **3**, 1–7 (2020).
45. Rodrigues, I. C., Bothner, D. & Steele, G. A. Coupling microwave photons to a mechanical resonator using quantum interference. *Nat. Commun.* **10**, 5359 (2019).
46. Zoepfl, D. et al. Kerr enhanced backaction cooling in magnetomechanics. *Phys. Rev. Lett.* **130**, 033601 (2023).
47. Bera, T., Majumder, S., Sahu, S. K. & Singh, V. Large flux-mediated coupling in hybrid electromechanical system with a transmon qubit. *Commun Phys* **4**, 1–7 (2021).
48. Diaz-Naufal, N. et al. Kerr-enhanced optomechanical cooling in the unresolved-sideband regime. *Phys. Rev. A* **111**, 053505 (2025).
49. Bothner, D., Rodrigues, I. C. & Steele, G. A. Four-wave-cooling to the single phonon level in Kerr optomechanics. *Commun. Phys.* **5**, 1–10 (2022).
50. Majumder, S., Bera, T. & Singh, V. Prospects of cooling a mechanical resonator with a transmon qubit in c-QED setup. *Phys. Rev. Res.* **4**, 033232 (2022).
51. Deeg, L. F. et al. Optomechanical backaction in the bistable regime. *Phys. Rev. Appl.* **23**, 014082 (2025).
52. Luschmann, T. et al. Mechanical frequency control in inductively coupled electromechanical systems. *Sci. Rep.* **12**, 1608 (2022).
53. Nation, P. D., Blencowe, M. P. & Buks, E. Quantum analysis of a nonlinear microwave cavity-embedded dc SQUID displacement detector. *Phys. Rev. B* **78**, 104516 (2008).
54. Aldana, S., Bruder, C. & Nunnenkamp, A. Equivalence between an optomechanical system and a kerr medium. *Phys. Rev. A* **88**, 043826 (2013).
55. Gardiner, C. W. & Collett, M. J. Input and output in damped quantum systems: Quantum stochastic differential equations and the master equation. *Phys. Rev. A* **31**, 3761–3774 (1985).
56. Ludwig, M., Kubala, B. & Marquardt, F. The optomechanical instability in the quantum regime. *New J. Phys.* **10**, 095013 (2008).
57. Degen, C. L., Reinhard, F. & Cappellaro, P. Quantum sensing. *Rev. Mod. Phys.* **89**, 035002 (2017).
58. Dhiman, S. et al. Self-Sustained Oscillations of a Nonlinear Optomechanical System in the Low-Excitation Regime (Data Archive). https://doi.org/10.5281/zenodo.18954807.
59. Dhiman, S. et al. Self-Sustained Oscillations of a Nonlinear Optomechanical System in the Low-Excitation Regime (Code Repository). https://doi.org/10.5281/zenodo.19627360.

Acknowledgements

All authors acknowledge funding from the Horizon Europe 2021–2027 Framework Programme under the Grant Agreement No. 101080143 (SuperMeQ). K.R., A.M., and H.H. disclose support from the Deutsche Forschungsgemeinschaft (DFG, German Research Foundation) under Germany's Excellence Strategy–EXC-2111-390814868. H.H. acknowledges funding from the Munich Quantum Valley, which is supported by the Bavarian state government with funds from the Hightech Agenda Bayern Plus.

Author contributions

S.D. and A. Me. developed the theoretical model, including its numerical solution. K.R. and T.L. performed the experiment and the experimental data analysis. H.H., T.L., and A.Ma. devised the experiment. S.D., K.R., A.Me., and H.H. wrote the manuscript with help from all authors.

Competing interests

The authors declare no competing interests.

Additional information

Supplementary information The online version contains supplementary material available at https://doi.org/10.1038/s41467-026-73259-x.

Correspondence and requests for materials should be addressed to A. Metelmann or Hans Huebl.

Peer review information *Nature Communications* thanks Gary Steele, who co-reviewed with Matteo ArfiniDong-Yang Wang and the other, anonymous, reviewers for their contribution to the peer review of this work. A peer review file is available.